

Characterizing the red optical sky background fluctuations from narrow-band imaging

M. Puech^a, H. Flores^a, Y.B. Yang^{a,b}, M. Rodrigues^{c,a,d}, T. Gonçalves^e, F. Hammer^a, and K. Disseau^a

^aGEPI, Observatoire de Paris, CNRS-UMR8111, Univ. Paris-Diderot, 5 place Janssen, 92195 Meudon, France

^bNational Astronomical Observatories, Chinese Academy of Sciences, 20A Datun Road, Chaoyang District, Beijing 100012, China

^cEuropean Southern Observatory, Alonso de Cordova 3107 - Casilla 19001 - Vitacura -Santiago, Chile

^dCENTRA, Instituto Superior Tecnico, Av. Rovisco Pais 1049-001 Lisboa , Portugal

^eObservatorio do Valongo, UFRJ, Ladeira Pedro Antonio, 43 - Saude, Rio de Janeiro-RJ, CEP 20080-090, Brazil

ABSTRACT

The detection and characterization of the physical properties of very distant galaxies will be one the prominent science case of all future Extremely Large Telescopes, including the 39m E-ELT. Multi-Object Spectroscopic instruments are potentially very important tools for studying these objects, and in particular fiber-based concepts. However, detecting and studying such faint and distant sources will require subtraction of the sky background signal (i.e., between OH airglow lines) with an accuracy of $\sim 1\%$. This requires a precise and accurate knowledge of the sky background temporal and spatial fluctuations. Using FORS2 narrow-band filter imaging data, we are currently investigating what are the fluctuations of the sky background at $\sim 9000\text{\AA}$. We present preliminary results of sky background fluctuations from this study over spatial scales reaching ~ 4 arcmin, as well as first glimpses into the temporal variations of such fluctuations over timescales of the order of the hour. This study (and other complementary on-going studies) will be essential in designing the next-generation fiber-fed instruments for the E-ELT.

Keywords: Extremely Large Telescope, Sky background, Sky subtraction, Imaging, Fiber spectrographs

1. INTRODUCTION

One of the prominent science cases for the future ESO 39 meter European Extremely Large Telescope (E-ELT)¹ is the detection and characterization of the first galaxies at very high redshifts ($z \leq 6$).² Spectroscopic observations of such small (half-light radii $R_{half} \sim 0.2$ arcsec) and faint ($J_{AB} \sim 26-27$) objects in the Near-Infrared (Y to Ks bands), will require accurate and precise background subtraction techniques at a level of one percent.³ This puts significant constraints on the instrument design concept and operations.

Fiber-fed instruments are often believed to suffer from a disadvantage in terms of sky subtraction accuracy compared to slits or image slicer IFUs. The two main drawbacks of fibers are thought to be their global throughput, which is limited by Focal Ratio Degradation (FRD), and the necessity of measuring the background signal several arcsec away of the scientific target because of the finite mechanical extension of the fiber buttons on the focal plane. While fiber-fed instrument can now offer global throughputs similar to those of slit spectrographs,³ it remains to be demonstrated that the background signal can be subtracted with an accuracy of at least one percent.

In this paper, we used narrow-band archive imaging data obtained with ESO-VLT/FORS2 to characterize the sky background spatial and temporal fluctuations. This should bring useful constraints on the maximal

Send correspondence to M. Puech: mathieu.puech@obspm.fr

distance between the scientific target and an associated fiber dedicated to measuring the sky background signal. In a companion paper, we also explored spectroscopic long-slit observations from ESO-VLT/FORS2.⁴ We also conducted on-sky tests of different sky background measurement and correction techniques using the multi-fiber optical spectrograph ESO-VLT/FLAMES-GIRAFFE.⁵ The reader is directly referred to these companions papers for further information on these on-going parallel studies.

2. OBJECTIVES AND METHODOLOGY OF THE STUDY

Very distant galaxies have their emission lines redshifted in the NIR. They are selected in order to target these lines between the very bright OH airglow sky lines. The detection success rate of very high- z faint sources is therefore driven by the accuracy on the measurement and subtraction of the sky background continuum between the OH sky lines. First tests on the sky subtraction strategy were conducted and are described elsewhere.⁵ In the present study, we focus on the measurement issue and we characterize the spatial and temporal sky background fluctuations in the continuum. Because longer wavelengths are more affected by thermal emission from the telescope and instrument, we decided to first investigate the red part of the optical domain ($\lambda \sim 900$ nm). Similar data at longer wavelengths will be explored in future studies.

We looked into the ESO raw data archive for programmes using narrow-band images at red optical wavelengths, and we find a number of ESO-FORS2 programmes suitable for our project. We further narrowed down the search to programmes that offered a large number of exposures with at least ~ 1 hr of continuous observations per night over several nights, and with large enough individual integration times (i.e., at least several minutes) to avoid the read-noise limited regime in the background. We ended up with two programmes particularly well-suited for our purposes, whose main characteristics are summarized in Tab. 1. We checked that no strong OH sky lines were in the spectral bandwidth of the two respective narrow-band filters, as shown in Fig. 1.

Table 1: ESO-VLT/FORS2 programmes used in the present study. *From left to right:* Programme ESO ID, programme PI, narrow-band filter used, central wavelength of the filter in nm, FWHM of the filter in nm, individual detector integration time DIT, and pixel size in arcsec.

ID	PI	Filter	λ_c	$\Delta\lambda$	DIT	Pixel
68.A-0182	A. Cimatti	z_SPECIAL	915	20	380	0.25
70.A-0591	E. Daddi	FILT_917_6	917	6	360	0.25

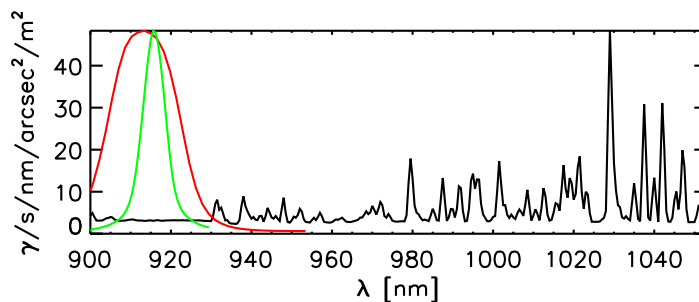


Figure 1: Narrow-band filters used in the archive data. A NIR sky background model for Mauna Kea is represented in black (airmass=1.5, middle of night). The red curve represents the z_SPECIAL transmission curve, while the green one represents the FILT_917_6 transmission curve (in arbitrary units).

3. DATA REDUCTION

We downloaded raw data from the ESO archive for the two programmes listed in Tab. 1. For homogeneity, we did not consider the first night (2001-24-11) of Prog. 68.A-0182 which was conducted before the change

of CCD in FORS2 that occurred in March 2002.⁶ We checked the availability of calibration frames (bias and twilight flat fields [hereafter FF]) in the archive for each night of both programmes. This led us to discard one night of Prog. 70.A-0591, because we were not able to retrieve daily bias frames for the remaining night, and one night (2002-10-07) of Prog. 68.A-0182, for which we were able to retrieve associated twilight FF frames.

3.1 Basic steps of data reduction

The basic steps of the standard reduction process were conducted using GASGANO⁷ and the associated ESO recipes. We first constructed master bias frames using the five to ten available daily raw bias frames in the archive. Master FF frames were also constructed using the associated four to five available daily twilight FF frames in the archive. Each individual raw frame was then reduced using standard procedures. We did not apply any dark correction since this is usually useless with FORS2 data⁸ but we checked that no particular spatial structure was imprinted in the dark frames available in the archive over the programme period. Reduced individual science frames were finally cut to remove the non-exposed part of the image and prevent possible edge effects during further steps. After visual inspection of the raw and reduced science frames, we systematically discarded data associated with the second (slave) CCD chip, since they were found to be more affected by cosmetic issues (e.g., bad pixels and/or columns). Regarding Prog. 68.A-0182, we further discarded data associated with the fourth night of the programme (2002-11-09), since they were affected by many satellite glows. This lets us with 35 frames spread over 4 nights (2002-10-08, 2002-11-11, 2003-02-03, and 2003-02-23). The individual frames sample periods of ~ 1 to 2 hr per night with sizes of approximately 7×4 arcmin². Regarding Prog. 70.A-0591, the final dataset is made of 63 raw frames, which sample periods of ~ 1 to 2 hr per night spread over four nights (2003-02-05, 2003-06-02, 2003-02-08, and 2003-10-02). Unfortunately, we were not able to retrieve associated daily twilight FF frames in the archive for this programme, so we used those taken on the 2003-09-02, which were used to construct a master FF frame. Since the four nights of observation considered were almost consecutive, we reduced all the individual frames using this master FF.

3.2 Background models and superflat-fielding

We used SWARP⁹ to combine all the dithered individual reduced science frames into master field mosaic images. SExtractor¹⁰ was then used to detect all the objects in these images. We used very low detection thresholds (0.3 to 0.7σ) combined to a Gaussian filter with large kernel (3 pixels FWHM) to ensure that the residual light from extended objects (galaxies) in the field is minimized. An additional morphological filtering was performed to enlarge the masks and limit the pollution by diffuse light at the edge of the objects in the field. Masks were projected back onto the individual reduced science frames, which were then normalized by the median value of the background (i.e., pixels not masked during the previous step). All normalized images were combined using a sigma-clipped median in the detector pixel frame (i.e., pixel-to-pixel) to produce a background model per night, in units of the median background level.

Each background model was analyzed using a wavelet decomposition¹¹ and visually inspected for possible additive features such as scattered light or fringing. Fringing at $\lambda \sim 900$ nm is expected at scales of ~ 40 pixels for the closest fringes,¹² and with peak-to-valley intensities of a few percent depending on exposure time.¹² Using a scale decomposition of a background model, one could in principle separate additive and multiplicative residual light as follows (see Fig. 2). The highest scales ($k=0-1$, which contain variations over $2^k=1-2$ pixels) allows us to characterize the noise and cosmetic properties (e.g., bad pixels and/or columns, noise patterns). The fringe pattern starts appearing at scales $k=2$ (variations over 4 pixels) and remains evident up to scale $k=6$ (i.e., variations over 64 pixels). The distance between the fringes is found to be 15-20 arcsec with peak-to-valley amplitudes of $\sim 0.1-0.3\%$ consistent with expectations at these wavelengths.¹² For both programmes, the fringe pattern is found to be significant only in the central bottom part of the CCD, where the density of galaxies in the field is the highest (see Fig. 3). Fringing is due to multiple reflections of quasi-monochromatic light between the surfaces of the CCD.¹³ Because it is associated to reflections and not to transmission effects in the instrument, it should in principle be corrected additively.¹⁴ One can therefore sum up the scale in which the variations are dominated by the fringe pattern ($k=2$ to 5), and subtract the result from the reduced frames. The residual large-scale variation can then be used as a second order multiplicative flat-field correction.

Background models revealed significant daily variations, so we did not consider long-term models but constructed daily background models. Given the limited number of calibration frames, each step of the data

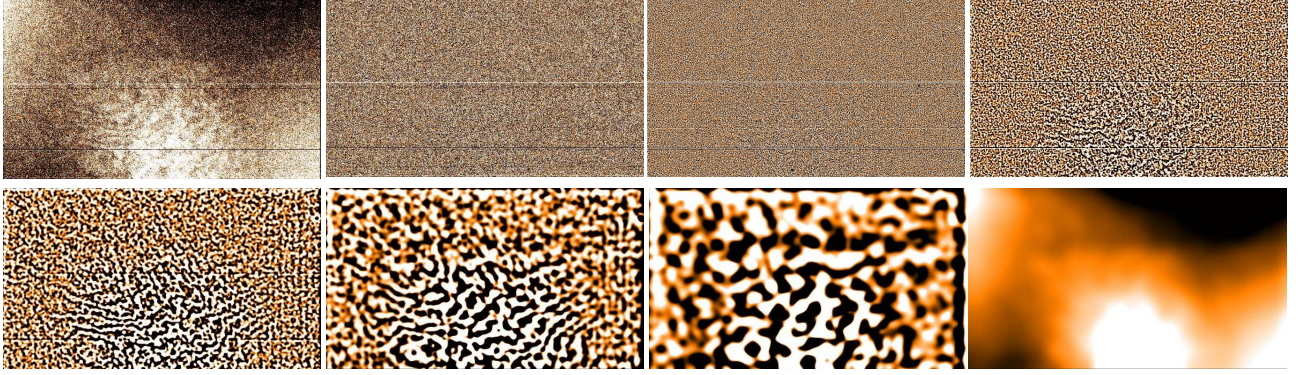


Figure 2: Scale decomposition of the background model for Prog. 70.A-0591. Here we show the background model constructed using all the reduced science frames, but daily background models were used to superflat the data. *From left to right and top to bottom*: background model, successive decomposition at scales 2^k pixels with $k=0-5$, and residual large-scale variations (subtraction of the $k=0$ to 5 scales from the background model).

reduction is likely to add significant noise to the individual science frames.^{14,15} Since the fringe pattern is found to be relatively weak, we chose not to apply an additive correction to save one reduction step and preserve the signal-to-noise ratio in the background. Instead, we treated the daily background model as a superflat used to apply a second-order flat-field multiplicative correction for both programmes. In doing so, one expects that sky background features should average in the detector frame, provided that their size is smaller than the image size. Such structures should therefore be preserved during the super-flatfielding correction. Further analysis of the background spatial fluctuations is therefore limited to scales that are typically smaller than half the image diagonal, according to the Nyquist-Shannon rule. For Prog. 68.A-0182 this translates into a maximal scale of ~ 240 arcsec. For Prog. 70.A-0591 we used the master field image produced using SWARP to define three rectangular regions around the central bottom region in the images where the fringe pattern is the strongest, as illustrated in the left panel of Fig. 3. We found a significant amount of diffuse light in this region which was indeed difficult to mask entirely using SEXTRACTOR because of the very high density of galaxies. Masking this region therefore prevents us to introduce large amounts of diffuse light in subsequent steps. Since we analyzed only three subregions, this programme allows us to characterize the spatial fluctuation of the background only up to scales ~ 140 arcsec.

The master field images resulting from the combination of all the super-reduced science frames are shown in Fig. 3. This figure illustrates that the limited number of dithered frames per night (typically 8-10 frames) did not allow us to construct complete superflat frames per night, i.e., superflat frames still contained blank pixels. These blank pixels result from regions that were masked on all the individual frames because of an extended bright object lying over these pixels in all the images.

3.3 Background continuum maps

To reduce the impact of noise on the background fluctuations, we “rebinned” the super-reduced science frames as follows. Using the master field images, a 2×2 arcsec² grid sampling the total observed field-of-view was constructed for each programme. This grid was projected back onto each super-reduced science image. Within each 2×2 arcsec² box of the grid, a sigma-clipped background median value was calculated to construct a background map for each individual science image. We therefore ended up with a set of background maps as a function of time with sampling of 2 arcsec. We show of few examples of such background maps in Fig. 4. Because we are interested only in relative fluctuations, we did not try to flux-calibrate the data. Since each super-reduced image was normalized by the median background value, the background maps allow us to characterize the fluctuations of the background signal *relative* to the median background value. We refer to other studies for an absolute characterization of the sky background continuum.¹⁶

We inspected the noise properties of the background maps before (0.25 arcsec/pix) and after rebinning (2 arcsec/pix). The median r.m.s. value before rebinning is found to be 3.9 and 16.4% of the median value

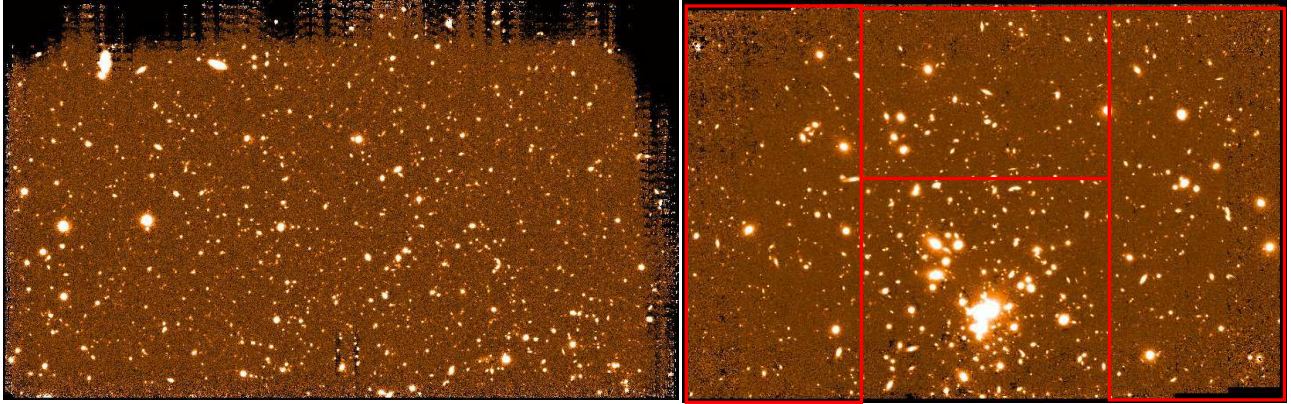


Figure 3: Master Fields (chip 1) of the two FORS2 programmes considered in this study. The master fields were constructed using SWARP from all the dithered super-reduced science frames. *Left*: programme 68.A-0182, for which all the field was analyzed. *Right*: programme 70.A-0591, for which only the three regions on the right, left, and top of the image (see red rectangles) were analyzed separately in order to avoid the densest region at the bottom center of the image (see text). Black pixels are pixels for which the superflats are incomplete due to the limited number of dithered science frames.

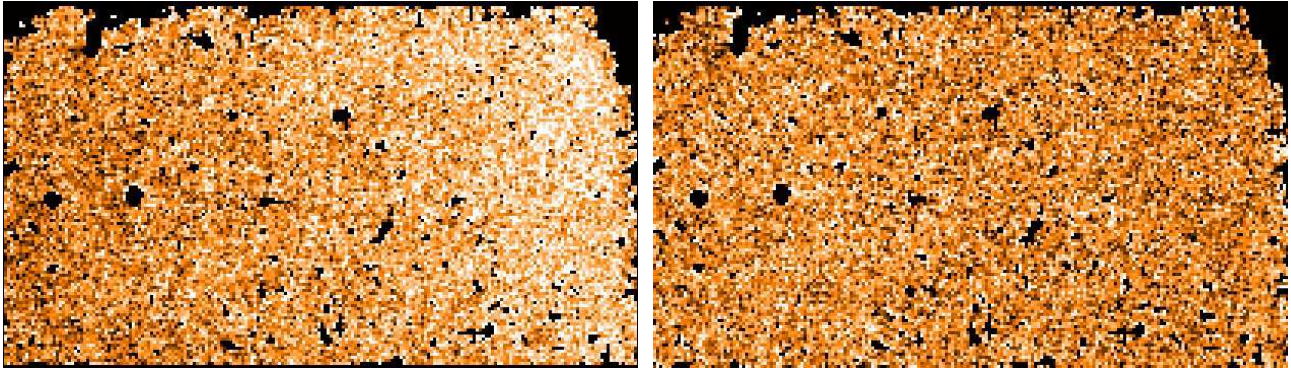


Figure 4: Two examples of background maps obtained using the programme 68.A-0182 (2 arcsec/pixel). Values are typically ranging between ~ 0.995 and 1.005 .

for Prog. 68.A-0182 and 70.A-0591 respectively. This difference should be in part due to the narrower filter and slightly shorter integration time used in Prog. 70.A-0591 (see Tab. 1), which are expected to result in a larger photon noise. The rebinning process should reduce the photon noise by a factor of at least $\sqrt{64}$, which should lead to r.m.s. values ~ 0.5 and 2% respectively. We measured the r.m.s. fluctuations in the rebinned background maps, which are found to be 0.3 and 0.8% respectively. The sigma-clipping used to generate background maps during the rebinning process therefore mitigates the photon noise efficiently. This suggests that background maps are not dominated by photon noise but by fluctuations at the smallest scale (see Fig. 4), although it cannot be excluded that residual photon noise still contribute to the r.m.s. fluctuations of the normalized background maps (see below).

Finally, we inspected visually all the super-reduced images as well as the daily superflat images and note that no concentric features were present. This suggests that the produced background maps are not dominated by scattered light or well-known sky concentration effects (i.e., light suffering multiple reflections between optical surfaces before reaching the detector), although it remains difficult to assess whether or not the background maps contain pure *sky* background signal or additional residual light from the instrument. However, analyzing such background maps may provide useful upper limits on the sky background fluctuations.

4. AUTOCORRELATION ANALYSIS OF THE BACKGROUND CONTINUUM MAPS

The autocorrelation function (ACF) of each background map was derived up to the limiting spatial scale (see above). In the following, we assume that the relative background signal is stationary over the considered temporal and spatial scales. We checked that the mean and r.m.s. relative background values were approximatively stable over the field-of-view, which suggests that the relative background signal is roughly stationary at least up to the second order, i.e., wide-sense stationary (WSS). We therefore assumed that the ACF depends on spatial shift only. Because the resulting ACFs are quite noisy, we considered daily median-averaged ACFs rather than individual ACFs. Since the individual exposure time and sampled period per night were more favorable for the programme 70.A-0591, we tentatively tried to construct hourly median-averaged ACFs for this programme only. We finally constructed two median-averaged ACFs considering all the frames of each programme, in order to check for possible systematics between the two different filters (see Fig. 5). In the following, we will refer to these different temporally average ACFs as daily, hourly, and total ACFs respectively. We now detail how median-averaged ACFs were constructed.

To mitigate the impact of noise, we used an iterative procedure to construct median-averaged ACFs. For each spatial scale, we derived the median value of the median-subtracted, r.m.s.-normalized set of relative background maps considered. The ACF of each individual background map ACF was then compared to the median ACF $Median_{ACF}$ using the following consistency function C :

$$C(scales) = \sum_{scales} \frac{(Median_{ACF} - ACF)^2}{Median_{ACF} \cdot N_{scales}}$$

The sigma-clipped median value C over all scales of $C(scales)$ was then derived. Every individual ACF having $C \geq 5$ was discarded. The process was iterated until no further rejection occurred. Tab. 2 lists the fraction of background maps discarded from the calculation of the median ACF per set of data considered. For Prog. 70.A-0591, the background maps corresponding to the three different regions extracted from the images were analyzed as distinct maps. Note that we did not average the data directly, which would have smooth out spatial features with short timescales. Instead, we averaged the ACF resulting of each background map, we should preserve statistically the spatial features of each background map. Table 2 shows that there is a non negligible variability of the ACF at all sampled timescales (0.5 to 3.5 hr). Given the relatively low signal-to-noise ratio of the relative background signal, it is difficult to test whether this variability can be attributed to pure background fluctuations or are due to noise fluctuations. However, in case of sky measurements using the offset technique, this suggests that the background signal should be sampled at timescales smaller than 0.5 hr, at least in the red optical ($\lambda \sim 900$ nm).

The median total ACFs are shown in Fig. 5 (see also Fig. 6). They show a very similar behavior, which suggests that the impact of using different filters is limited. Figure 5 also shows the ACFs that were rejected during the median calculation. All rejected ACFs show a trend to larger correlations at all scales.

We compare the total, daily, and hourly ACFs in Fig. 6. Daily ACFs show consistent behavior except for two nights in Prog. 68.A-0182 (2002-10-08 and 2003-03-23) where larger correlations over all scales are detected. This shows that such a systematic increase in correlation at all scales can be transitory but also stable over at least one hour.

5. SPATIAL AND TEMPORAL FLUCTUATIONS OF THE BACKGROUND CONTINUUM

5.1 Sizes and amplitudes of fluctuation scales

In order to further quantify the fluctuations of the relative background signal, we fitted the ACFs corresponding to different datasets as follows. We first generated Gaussian Random Fields (GRFs) on a 200×200 pixel grid. We combined several GRFs of different scales (defined as the FWHM of the Gaussian kernel used to generate the GRF) and amplitudes (in units of the median background signal), and calculate the resulting ACF. The scales

Table 2: Rejection rate of the iterative procedure used to construct the median ACFs for each dataset. *From left to right*: Dataset (Total = all background maps for a given programme, YYYY-MM-DD = all maps for a given night/programme), YYYY-MM-DDTHH = all maps within HH to HH + 1 hr of a given night/programme), rejection rate in %, remaining number of background maps used to construct the ACF, and approximative timescale sampled by the individual maps in hr.

70.A-0591				68.A-0182			
DataSet	Rejection rate	N_{ACF}	Timescale	DataSet	Rejection rate	N_{ACF}	Timescale
Total	46%	166	–	Total	12%	19	–
2003-02-05	11%	24	1	2002-10-08	9%	10	1
2003-02-06	22%	42	2	2002-11-11	0%	8	1
2003-02-08	16%	63	3.5	2003-02-03	0%	8	1
2003-02-10	4%	26	1	2003-02-23	0%	8	1
2003-02-05T07	0%	15	0.5				
2003-02-05T08	0%	12	0.5				
2003-02-06T07	29%	17	0.5				
2003-02-06T08	8%	22	0.5				
2003-02-06T09	0%	6	0.5				
2003-02-08T05	8%	11	0.5				
2003-02-08T06	11%	24	0.5				
2003-02-08T07	7%	14	0.5				
2003-02-08T08	10%	19	0.5				
2003-02-10T07	0%	18	0.5				
2003-02-10T08	0%	9	0.5				

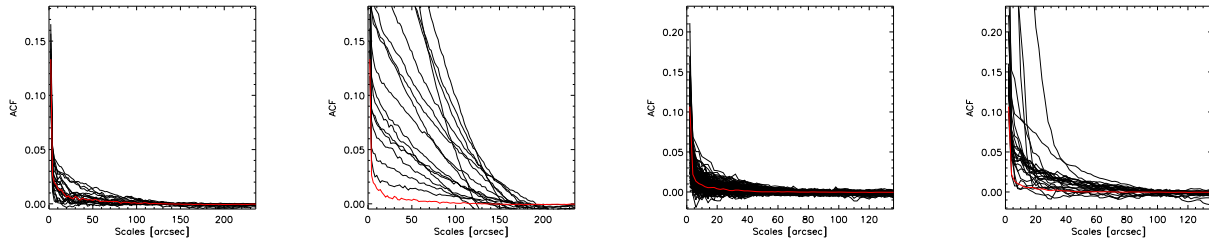


Figure 5: *From left to right*: total 68.A-0182 ACF and rejected ACFs for Prog. 68.A-0182 and 70.A-0591 respectively. Black lines in the first and third panels represent ACFs derived from individual background maps that were not rejected by the consistency criterion (see text), while the red line is the corresponding median ACF. Black lines and the second and fourth panels show the ACFs rejected by the consistency check criterion, while the red line is the median ACF from the first and third panels. The value of the ACFs at origin was not plotted for visualization ease ($ACF(0)=1$).

and amplitudes of the combined GRFs were then fitted to a given median observed ACF using a Levenberg-Marquardt χ^2 minimization scheme. We used the $1\text{-}\sigma$ scatter around the median ACF as uncertainties during the fitting process. We find that at least three GRFs were needed to provide a satisfying fitting, while more GRFs did not provide any significant improvement. We also tried to directly fit the ACF shape using a set of three Gaussian distributions assuming uncorrelated Gaussian fluctuations, but we found that the result were less accurate that with fitting GRFs.

The fitted scales and amplitudes of all observed median ACFs are shown in the left panel of Fig. 8. Scales are directly inferred from the fitted GRF FWHMs, while amplitudes are derived using the respective weight of each GRF to the total variance of the surface used to fit the ACF. To translate these relative weights into absolute contributions in fractions of the median observed background, we rescaled each weight by the median

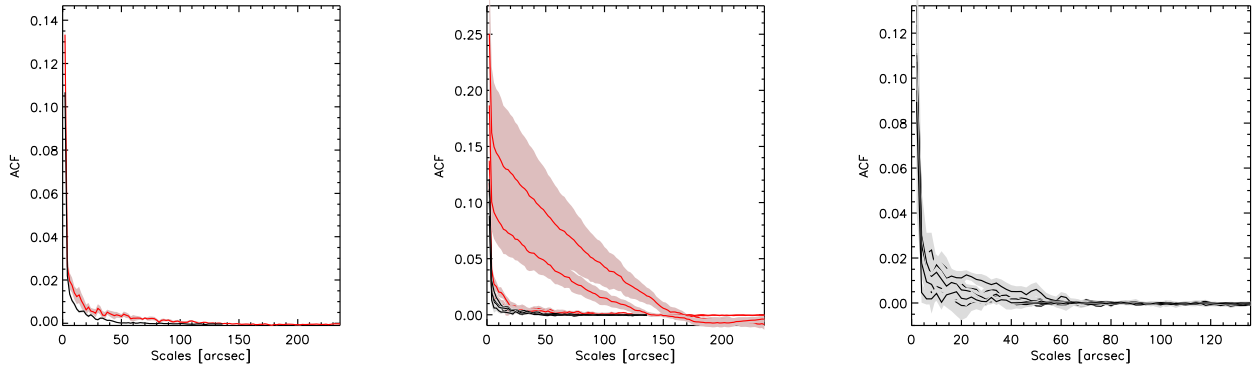


Figure 6: Comparison between the total (left panel), daily (middle panel), and hourly (right panel) median ACFs. The red lines shows ACFs for the 68.A-0182 programme, while the black lines show ACFs for the 70.A-0591 programme. Uncertainties on the median ACFs (as derived from bootstrap resampling) are shown as gray or light red areas.

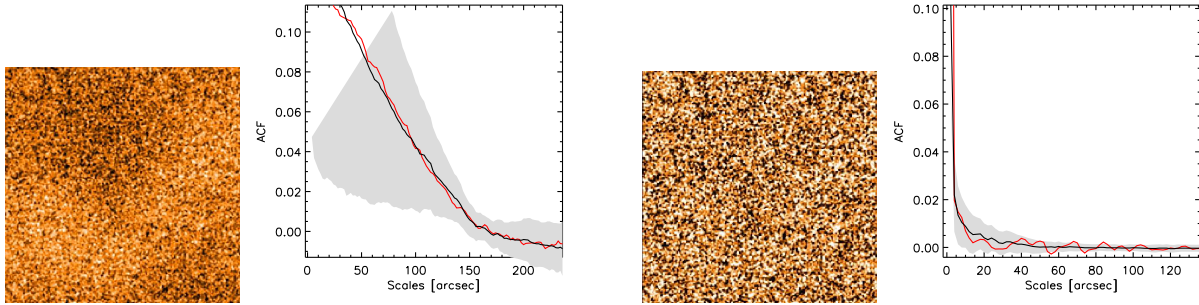


Figure 7: Two examples of combination of three GRFs used to produce fake background fluctuation maps that fit observed ACFs. *From left to right:* simulated background map used to fit the 2002-10-08 median ACF in Prog. 68.A-0182, corresponding median ACF (black curve) with associated scatter (gray area) and fitted ACF derived from the simulated map (red line), simulated background map used to fit the total 70.A-0591 ACF, corresponding ACF with associated uncertainty and fitted ACF. The simulated background maps are to be compared visually to those shown in Fig. 4. Note that the map on the left is one of those that show unusually large correlations at all scales (see text).

r.m.s. of all background maps. Fig. 8 suggests that three distinct scales are always present in the data. The smallest scale, but largest in amplitude, appears to have limited variations in amplitude centered around two typical values, i.e., ~ 0.7 and $\sim 0.32\%$. This probably reflects the fact that background maps for Prog. 70.A-0591 still contain significant photon noise (see Sect. 3.3) and that the real amplitude of the smallest scale is closer to 0.3%, or even smaller. We emphasize that all absolute levels of amplitude has to be taken as upper limits only, since they were derived from the measured median r.m.s. fluctuations of the background maps. As discussed in Sect. 3.3, we indeed cannot exclude that these maps still contain significant fluctuations associated to photon noise. The two largest scales reveal amplitudes which are one order of magnitude smaller. The intermediate scale at ~ 30 arcsec appears to be relatively well defined in size, while the largest one appears to be of the order of ~ 70 arcsec on average, although the data are scattered over a large range. The median size and amplitude of the three scales are listed in Tab. 3.

5.2 Possible origin of the fluctuation scales

To investigate the origin of the smallest scale, we plot in the right panel of Fig. 8 the size of the smallest scale as a function of the mean expected image quality in the corresponding dataset. Image quality was estimated by converting the seeing values recorded into the file headers into image FWHM.¹⁷ All FWHMs were derived

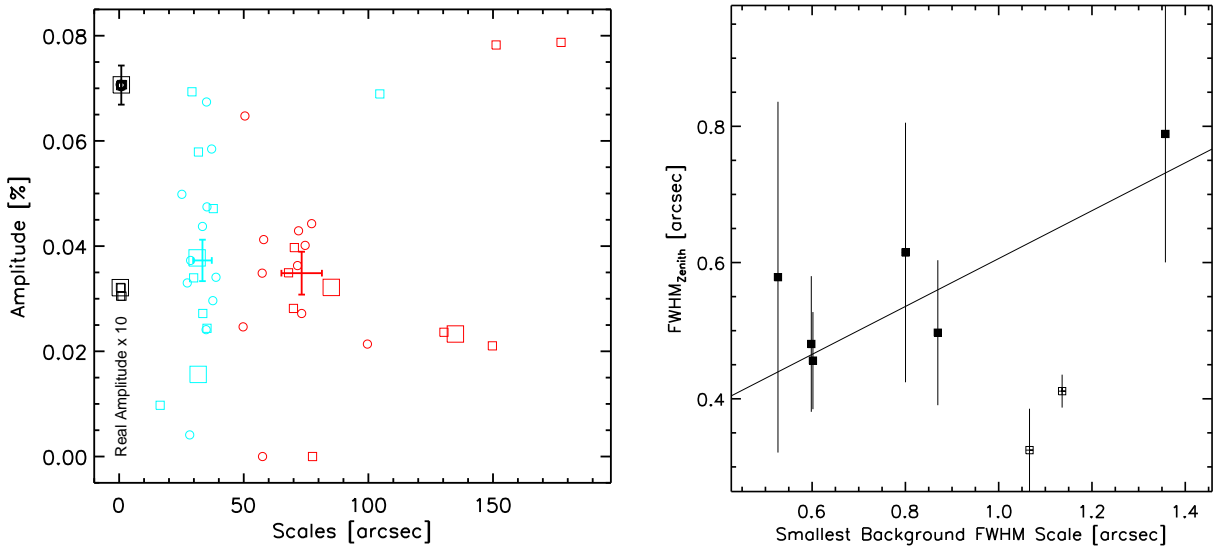


Figure 8: *Left*: Result of the fitting of three GRFs to the background map ACFs. Amplitudes are given in % relative to the median background value, while scales correspond to the GRF FWHMs in arcsec. Black symbols represent the smallest fitted scale (their amplitude were divided by a factor ten for visualization ease), blue symbols represent the intermediate fitted scale, while red symbols represent the largest fitted scale. Empty circles represent hourly datasets, small empty boxes represent daily datasets, and large empty boxes represent total datasets, while crosses represent median values per scale with associated uncertainty. *Right*: Expected image quality FWHM at zenith and 916nm as a function of the smallest FWHM scale (both in arcsec) for the daily datasets. The error-bars represent the $1\text{-}\sigma$ scatter derived within each dataset, while the black line is a linear fit to the data, taking into account only full symbols.

Table 3: Median scales (FWHM in arcsec) and amplitudes (in % relative to the median background value) of the three dominant scales of the relative background fluctuations as inferred from Fig. 8. Note that the amplitude of the smallest is probably closer to $\sim 0.32\%$, or even smaller (see text).

	Smallest scale	Intermediate scale	Largest scale
Scale	0.86 ± 0.06	33.43 ± 3.65	73.23 ± 8.01
Amplitude	0.71 ± 0.04	0.04 ± 0.01	0.04 ± 0.01

at $\lambda=916\text{nm}$, which is approximatively the center of the two narrow-band filters considered, and homogenized at zenith using the mean airmass in the dataset. A turbulence outer scale of 8m (i.e., the telescope pupil diameter) was used during the fit.¹⁷ If one discards the two points with smallest image quality FWHM, the probability that the two quantities are correlated is found to be $\sim 92\%$. This suggests that the smallest scale of the background fluctuations is probably linked to atmospheric turbulence effects*.

The largest scale of fluctuation is found to be ~ 70 arcsec on average with large scatter. The largest fluctuations (in size) of the atmosphere are known to be due to gravitational waves in the mesosphere.¹⁸ However, such waves reveal wavelengths of several degrees and r.m.s. variations of $\sim 3\text{-}4\%$.¹⁸ It is therefore unlikely that such fluctuations might be linked to the largest fluctuations at ~ 70 arcsec. A more likely explanation for these fluctuations is a known multiplicative feature that can appear in the FF frames and varies as a function of the angle of the field rotator.⁶ The number of twilight FF frames available (see above) is clearly too low to smooth out this pattern, which might therefore let an imprint in the background maps. Such a pattern is

*which might be related to scintillation. Such a possible link is beyond the scope of the present study and will be explored in future studies.

indeed found to dominate in amplitude the FF variations at scales larger than ~ 70 arcsec.⁶ This might be a natural explanation for the large range of values found at the largest scales (~ 50 to 180 arcsec), as a result of the random combination of the field rotator angle between the individual frames and twilight FF frames.

The intermediate scale is found to be close to ~ 30 arcsec. Since we did not correct the fringe pattern explicitly but only applied a multiplicative correction (whereas the fringe pattern is additive), such a scale could be associated to fringing residual light. However, the inter-fringe distance is found to be 15-20 arcsec with amplitudes ~ 0.1 - 0.3% . These sizes and amplitudes are significantly different that what is found for the intermediate-scale fluctuations with FWHM sizes ~ 25 - 40 arcsec and amplitudes mostly in the range 0.02-0.07%. We conclude that our multiplicative correction of the fringe pattern is accurate enough and that the intermediate-scale fluctuations of the background are probably not related to fringing. Moreover, fluctuations at these scales are too small to be associated to the feature introduced by the field rotator angle as discussed above.⁶ So far, it remains unclear to what process(es) fluctuations at these scales could be associated, and whether these fluctuations are associated to sky background fluctuations or instrument residual light.

5.3 Limitations and future plans

One should consider the above results as characterizing the fluctuations of the global background, i.e., potentially including residual scattered light or flat field effects, rather than pure sky background. The possible link between the largest scale fluctuations and the field rotator scattered light indeed suggests that the background maps could be polluted with residual instrumental effects. However, we found that amongst the three scales that emerge systematically from the ACF associated to these fluctuations, at least one of them could be associated with atmospheric effects (i.e., turbulence). This gives us some confidence that the present results provide at least upper limits on the sky background relative fluctuations. To confirm these results, it will be very useful to analyze more narrow-band imaging data obtained with other instruments. Finding similar scales and amplitudes with other datasets from another instrument would strongly suggest that the results of the present study are not limited by instrument residuals but truly characterize the real sky background fluctuations.

Finally, direct on-sky tests conducted on fiber-fed spectrographs are on-going.⁵ Preliminary results using FLAMES-GIRAFFE at VLT suggest that a sky background measurement conducted ~ 10 - 15 arcsec away from the scientific fiber is sufficient to subtract the sky signal with an accuracy of one percent. According to the results of the present study, measurements at such a scale should indeed provide a signal correlated with all large-scale fluctuations. Sky subtraction should therefore be limited by fluctuations at the smallest scale, which will remain hardly measurable in parallel to scientific observations, even with slit spectroscopy. We found typical amplitudes of a few tenth of percent at this scale, consistent with a limit on the sky background subtraction accuracy of $\sim 1\%$ on the continuum as suggested by on-going on-sky tests.⁵ We emphasize that such on-sky tests were conducted using a fiber-fed spectrographs, which therefore suggests that such instruments can be as accurate as slit spectrographs for sky subtraction procedures.

6. CONCLUSION

We have analyzed ESO FORS2 archive narrow-band imaging data at $\lambda \sim 0.9\mu m$ to characterize the temporal and spatial fluctuations of the sky background. We carefully reduced two archive programmes that sample timescales in the range 0.5-3.5 hr and spatial scales up to 240 arcsec. The limited signal-to-noise ratio and possible non-identified residual flat field and/or scattered light effects are clear limitations to such an exercise. Assuming that upper limits on the total background fluctuations can nevertheless be derived, we summarize our results as follows:

1. Background fluctuations show, as expected, random spatial and temporal behaviors. Large variations in the spatial correlation are observed at all the sampled timescales. Nevertheless, a dominant behavior in the spatial fluctuations appears to emerge.
2. Relative spatial fluctuations of the background (relative to the median background value) is found to be dominated by three distinct scales. All these fluctuations result in total r.m.s. variations below one percent.

3. The smallest scale dominates in term of amplitude ($\sim 0.3\%$), which is found to be one order of magnitude larger than the two largest scales. This scale could be related to atmospheric turbulence.
4. The largest scale fluctuates at amplitudes of $\sim 0.035\%$. This spatial scale shows large variations in size, with values between 50-180 arcsec in the present study. These fluctuations could be linked with scattered light depending on the field rotator angle.
5. The intermediate scale is found to be well defined at ~ 30 arcsec with amplitudes similar to those of the largest scale. It is unlikely that these fluctuations are related to fringing or the field rotator effect. It remains unclear to what process(es) such fluctuations could be associated.
6. From an instrument design point of view, this study suggests that sky background continuum fluctuations should be sampled over timescales significantly below 30 min and on spatial scales significantly below 30 arcsec. Fluctuations at the smallest scale are probably limiting any sky background measurement/subtraction technique, even with slit spectrographs. We found that fluctuations at this scale have amplitudes of a few tenth of percent, which likely represent a lower bound to the accuracy one can reach in term of sky subtraction with spectroscopic observations.
7. Results from on-sky tests suggest that a limit of 1% in accuracy of the sky subtraction process can already be reached on existing red-optical spectrograph, including fiber-fed instruments. Further tests will be needed before generalizing this result in the NIR regime, in which residual light from thermal emission background will be an additional source of additive residual light and will therefore further limit the accuracy one can reach of the sky subtraction process.

ACKNOWLEDGMENTS

We thank all ESO staff contributing to maintain the raw data archive, which was extensively used in this study.

REFERENCES

- [1] Gilmozzi, R. and Kissler-Patig, M., “The E-ELT has Successfully Passed the Phase B Final Design Review,” *The Messenger* **143**, 25–25 (2011).
- [2] Evans, C., “Multi-Object Spectroscopy with the European ELT: Synergies between EAGLE & EVE,” *Society of Photo-Optical Instrumentation Engineers (SPIE) Conference Series* **8446** (July 2012). These proceedings.
- [3] Navarro, R., Chemla, F., Bonifacio, P., Flores, H., Guinouard, I., Huet, J.-M., Puech, M., Royer, F., Pragt, J. H., Wulterkens, G., Sawyer, E. C., Caldwell, M. E., Tosh, I. A. J., Whalley, M. S., Woodhouse, G. F. W., Spanò, P., di Marcantonio, P., Andersen, M. I., Dalton, G. B., Kaper, L., and Hammer, F., “Project overview of OPTIMOS-EVE: the fibre-fed multi-object spectrograph for the E-ELT,” *Society of Photo-Optical Instrumentation Engineers (SPIE) Conference Series* **7735**, 88 (2010).
- [4] Yang, Y., “The variations of sky continuum background at Near IR band,” *Society of Photo-Optical Instrumentation Engineers (SPIE) Conference Series* **8446** (2012). These proceedings.
- [5] Rodrigues, M., “Multi-Object Spectroscopy with the European ELT: Synergies between EAGLE & EVE,” *Society of Photo-Optical Instrumentation Engineers (SPIE) Conference Series* **8450** (2012). This conference.
- [6] Moehler, S., Freudling, W., Møller, P., Patat, F., Rupprecht, G., and O’Brien, K., “Correction of Field Rotator-Induced Flat-Field Systematics - A Case Study Using Archived VLT-FORS Data,” *PASP* **122**, 93–102 (2010).
- [7] Izzo, C., Kornweibel, N., McKay, D., Palsa, R., Peron, M., and Taylor, M., “Gasgano & ESO VIMOS Pipeline released,” *The Messenger* **117**, 33–35 (2004).
- [8] O’Brien, K., “Fors1+2 data reduction cookbook,” *ESO* (2007).
- [9] Bertin, E., “SWarp: Resampling and Co-adding FITS Images Together,” *Astrophysics Source Code Library*, 10068 (2010).
- [10] Bertin, E. and Arnouts, S., “SExtractor: Software for source extraction.,” *A&AS* **117**, 393–404 (1996).

- [11] Starck, J.-L. and Murtagh, F., [*Astronomical Image and Data Analysis*], Springer-Verlag.
- [12] Walsh, J. R., Kuntschner, H., Jehin, E., Kaufer, A., O'Brien, K., Riquelme, M., and Smette, A., "Modelling the Fringing of the FORS2 CCD," *2007 ESO Instrument Calibration Workshop*, 63 (2008).
- [13] Howell, S. B., "Fringe Science: Defringing CCD Images with Neon Lamp Flat Fields," *PASP* **124**, 263–267 (2012).
- [14] Gullixson, C. A., "Two Dimensional Imagery," in [*Astronomical CCD Observing and Reduction Techniques*], Howell, S. B., ed., *Astronomical Society of the Pacific Conference Series* **23**, 130 (1992).
- [15] Newberry, M. V., "Signal-to-noise considerations for sky-subtracted CCD data," *PASP* **103**, 122–130 (1991).
- [16] Cuby, J. G., Lidman, C., and Moutou, C., "ISAAC: 18 Months of Paranal Science Operations," *The Messenger* **101**, 2–8 (2000).
- [17] Tokovinin, A., "From Differential Image Motion to Seeing," *PASP* **114**, 1156–1166 (2002).
- [18] High, F. W., Stubbs, C. W., Stalder, B., Gilmore, D. K., and Tonry, J. L., "Sky Variability in the y Band at the LSST Site," *PASP* **122**, 722–730 (2010).